Simulations of Dedicated LEO-PNT Systems for Precise Point Positioning: Methodology, Parameter Analysis, and Accuracy Evaluation

FABRICIO S. PROL
M. ZAHIDUL H. BHUIYAN
SANNA KAASALAINEN
National Land Survey of Finland, Espoo, Finland

E. SIMONA LOHAN, Senior Member, IEEE
Tampere University, Tampere, Finland

JAAN PRAKS
Aalto University, Espoo, Finland

KAAN ÇELIKBILEK
Tampere University, Tampere, Finland

HEIDI KUUSNIEMI, Member, IEEE
National Land Survey of Finland, Espoo, Finland
University of Vaasa, Vaasa, Finland

Manuscript received 9 December 2022; revised 30 May 2023, 22 December 2023, and 11 March 2024; accepted 19 May 2024. Date of publication 24 May 2024; date of current version 11 October 2024.

DOI. No. 10.1109/TAES.2024.3404909

Refereeing of this contribution was handled by Z. (Zak) Kassas.

This work was supported by the Technology Industries of Finland Centennial Foundation and the Jane and Aatos Erkko Foundation through the INdoor navigation from CUBesAT Technology project.

Authors' addresses: Fabricio S. Prol, M. Zahidul H. Bhuiyan, and Sanna Kaasalainen are with the Department of Navigation and Positioning, Finnish Geospatial Research Institute, National Land Survey of Finland, 02150 Espoo, Finland, E-mail: (fabricio.dossantosprol@nls.fi); E. Simona Lohan and Kaan Çelikbilek are with the Electrical Engineering Unit, Faculty of Information Technology and Communication Sciences, Tampere University, 33720 Tampere, Finland; Jaan Praks is with the Department of Radio Science an Engineering, Aalto University, 02150 Espoo, Finland; Heidi Kuusniemi is with the Department of Navigation and Positioning, Finnish Geospatial Research Institute, National Land Survey of Finland, 02150 Espoo, Finland, and also with the Digital Economy Research Platform and the School of Technology and Innovation, University of Vaasa, 65101 Vaasa, Finland. *(Corresponding author: Fabricio S. Prol.)*

Low earth orbit (LEO) satellites provide the potential to overcome the current limitations in global navigation satellite systems (GNSSs) due to the increased satellite velocity and signal reception power. As the whole LEO segment grows, preliminary studies and simulations have been conducted in the most recent years to identify how to develop a LEO positioning, navigation, and timing (PNT) system and add value to the GNSS. To promote the development of LEO-PNT, this work presents the simulation of several key components of a dedicated LEO-PNT system. Our investigation analyzes features of the satellite constellation, orbits, onboard instruments, signal propagation effects, and user measurements and maps the accuracy of the service on the ground. The analysis considers the signal propagation from both LEO and medium earth orbit satellites and provides the expected accuracy of a ground user when certain system parameters and instruments are defined in the space mission design. All parameters and statistical distributions, which can serve to future LEO-PNT simulations and developments, are presented. For validation and demonstration, a comparison is presented to analyze the expected positioning errors for LEO satellites and how they differ from the classic GNSS. Our investigation enables a valuable quantitative analysis of the dedicated LEO-PNT systems and provides analysis for LEO-PNT system design optimization.

I. INTRODUCTION

High-altitude orbits above 10 000 km from ground have been normally used in satellite communications and satellite navigation, as the high orbit can provide large service coverage area and fixed services. The drawback of a high-orbit satellite is the weak signal level and significant delay in communication. Satellites placed in low earth orbit (LEO), i.e., at around 400–1200 km above the sea level, in contrast, provide much better signal properties, but the very high number of satellites needed for global coverage has kept this option unrealistic. In recent years, the development in satellite miniaturization, mass production, and launch technology has decreased the prices drastically and LEO-based satellite services have started to grow rapidly.

LEO satellites provide better services than traditional satellites at higher orbits in several application areas of wireless communications. There is now a worldwide growing interest toward a similar paradigm shift also in navigation, with the goal of providing positioning, navigation, and timing (PNT) through LEO satellites [1], [2], [3], [4]. This concept to perform navigation, nowadays referred to as LEO-PNT, can provide benefits in comparison to classic global navigation satellite systems (GNSSs) placed in medium earth orbit (MEO), since LEO satellites can offer fast geometric change [5], [6] and increased signal reception power [7]. The PNT solution can be derived from satellite constellations designed for Internet-of-Things connectivity, communication [8], earth observation, or those fully dedicated to PNT. Among these options, the latter provides the highest level of accuracy [9]. However, to date, there have been no dedicated LEO-PNT systems completely operational, so that mission designs are essential, especially in the face of the continuously growing number of LEO satellites [10].

A reasonable constellation design is one of the most relevant issues still to be settled in dedicated LEO-PNT systems [11], as it defines the service geometry and amount of

TABLE I
Expected Components for an End-to-End Simulation Tool of a LEO-PNT Navigation System, Contrasted With Our Simulator

Component	Relevant Features of an End-to-End Simulator	Our Simulator
1. Satellite Constellation	Constellation Topology, Number of Planes, Number of Satellites per Plane, Orbit Inclination, Orbit Altitude, Orbit Eccentricity, Orbit Propagation	All Included
2. On-Board Instruments	Navigation Payload, GNSS Payload, Communication Payload, Platform Design, Power Supply, Attitude Control	Navigation Payload GNSS Payload
3. Orbit Determination	Single Point Positioning (SPP), Kinematic POD, Dynamic POD, Reduced-Dynamic POD	SPP, Kinematic POD
4. Signal Design	Modulation, Multiple-Access, Channel Coding, Beamforming, Frequency	Frequency
5. Signal Propagation Effects	Instrumental Delay, Ionospheric Delay, Ionospheric Scintillation, Tropospheric Delay, Tropospheric Scintillation, Multipath, Signal Attenuation, Signal Obstruction	Instrumental Delay Ionospheric Delay Tropospheric Delay
6. Ground-Segment Architecture	Communication Links, Optimization Strategy of Antenna Locations	None
7. User Measurements	Carrier Phase, Pseudorange, Doppler-shift, Signal-to-Noise Ratio (SNR), In-Phase and Quadrature Data	Carrier Phase, Pseudorange, Doppler-shift
8. User Positioning	Doppler-Based Positioning, SPP, PPP, Differential Positioning, Hybrid Positioning with, i.e., Inertial Measurement Unit (IMU)	Doppler-based positioning, SPP, PPP
9. User Application	Antenna Design, Receiver Design, Accuracy, Integrity, Availability, Continuity, Coverage	Accuracy, Coverage

needed satellites. The satellite constellation orbital configuration is usually defined by running a set of complex algorithms to simulate the space-segment orbital geometry [12]. Several features, such as orbit inclination, orbit altitude, platform speed, and possible onboard instruments, should be analyzed to optimize the service coverage, cost, and end-user accuracy. A complete LEO-PNT system simulation also requires accounting for the signal propagation effects, ground segment design, and user segment properties. In this regard, most of the current simulations have focused on fragmented topics of the full-chain LEO-PNT solution [9]. They have focused on how to define new orbit models embedded to the broadcast messages [13], [14], [15], orbit determination [16], [17], [18], signal structure designs [19], [20], [21], atmospheric models [22], [23], [24], constellation optimization strategies to improve the GNSS convergence time [6], [25], satellite clocks [26], [27], user performance estimation [28], [29], [30], [31], [32], [33], [34], and integration with distinct sensors [35]. To expand the simulations, there is still a gap in the process of implementing an end-to-end LEO-PNT system, binding all segments in a unified model. To the best of the authors' knowledge, there is currently no single commercial or scientific simulator available that offers a complete LEO-PNT solution, incorporating all the essential components, such as space, ground, and user segments.

This article presents results of a comprehensive simulation of various components of a dedicated LEO-PNT system. The simulation offers insights into the performance and accuracy of the LEO-PNT system for precise point positioning (PPP) in the postprocessing mode. The simulations cover essential observations used in satellite-based PNT, such as pseudorange, carrier phase, and Doppler-shift measurements, and evaluate the model's ability to reproduce them accurately. By defining the techniques and parameter intervals based on experimental data analysis, this work not only contributes to the development of LEO-PNT systems but also serves as a valuable resource for future simulations. Table I outlines the expected components of an end-to-end simulator, contrasting them with the functionalities currently enabled in our existing simulator. It is essential to acknowledge that a fully simulated end-to-end environment has not been attained due to the inclusion of approximations in the simulation setup. Nevertheless, our simulations bring us significantly closer to this objective.

The article follows a similar structure to [9], providing a comprehensive view of the three LEO segments (space, ground, and user) as well as the considerations of the signal propagation. In [9], the analysis is primarily based on a literature review, whereas our study relies on an in-house simulation tool. As a result, we are able to validate and reinforce certain aspects discussed in previous works. In addition, while Prol et al. [9] speculate about possible requirements of LEO-PNT systems, our article provides concrete numerical values to support our analysis, while also uncovering novel findings.

We present new findings on the impact of upcoming LEO-PNT systems on PPP. Drawing upon historical data from the International GNSS Service (IGS), we explore various scenarios, ranging from user to space segment perspectives, to discern how PPP would be influenced. Specifically, this article delves into the following key points.

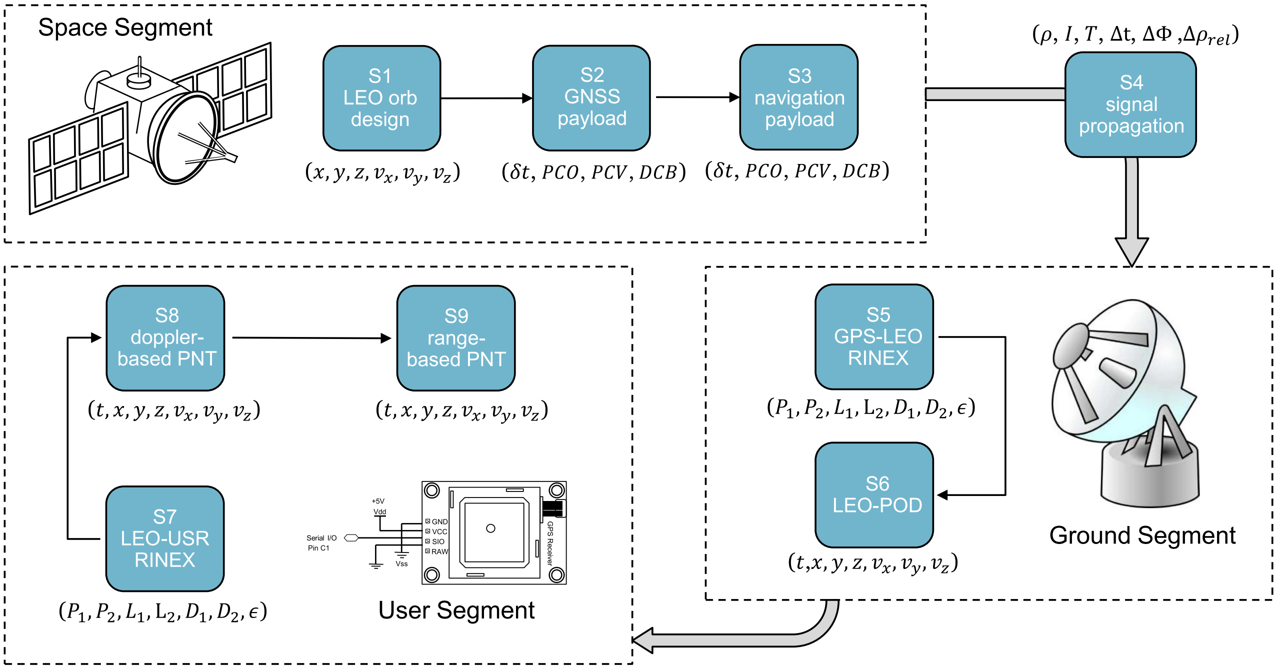

Fig. 1. LEO-S9: model with nine modules to represent the LEO-PNT space segment, signal propagation, ground segment, and user segment.

1) Our findings corroborate certain aspects observed in prior research, such as the satellite constellation design required in dedicated LEO-PNT systems, expected precise orbit determination (POD) accuracy, and foreseen benefits that LEO satellites can bring to PPP.
2) We investigate the impact of numerous factors on LEO-PNT measurements, encompassing orbital errors, earth's rotation effects, satellite rotation impacts, relativistic effects, and atmospheric delays.
3) We examine the expected accuracy of single-frequency pseudorange measurements when employing a high-accuracy 3-D ionospheric model.
4) We explore the precision of LEO interpolation, utilizing a technique commonly employed in PPP to estimate GNSS satellite orbits.

The main assumption of our investigation is that the LEO satellites are designed with specifications similar to those of global positioning system (GPS) satellites operating at lower orbits, including the signal frequency, beamforming techniques, system accuracy, and other relevant aspects, which are elaborated in the following sections. This assumption holds practical relevance in the upcoming years, given the ongoing developments of satellite missions using "GPS-like" signals in LEOs, as exemplified by CentiSpace [36], [37] and underdevelopment projects, such as the Xona's Pulsar system [38], the LEO-PNT system by the European Space Agency [39], and our project focused on indoor navigation using CubeSat technology (INCUBATE) [40]. Another pertinent point of the study is that POD is conducted within the ground segment in the postprocessing mode. It is presumed that data distribution occurs through an Internet connection, thereby excluding real-time users and those without internet connectivity.

II. LEO-S9 MODEL OVERVIEW

LEO-S9 (LEO simulator with nine modules) is the name given to our simulator, as it is based on nine modules. The diagram in Fig. 1 illustrates the sequential process of the LEO-S9 simulator. This diagram is not intended to represent a real LEO-PNT system. Its primary purpose is to demonstrate the sequential order of the modules from 1 to 9. The four main parts of a satellite-based navigation system are reproduced in the model: the space segment, the signal propagation effects, the ground segment, and the user segment.

The space segment simulates the LEO dynamics and the satellite payloads. Main model parameters consider the metrics that affects the system accuracy, such as orbits, clocks (δt), instrumental biases, such as the differential code bias (DCB), and antenna design, including frequencies, phase center offset (PCO), and phase center variation (PCV).

The signal propagation module provides the geometric distances (ρ), ionospheric (I) and tropospheric (T) delays, signal propagation time (Δt), phase windup ($\Delta\Phi$), and relativistic effects ($\Delta\rho_{\text{rel}}$). Several options exist for signal modulation, channel coding, and multiple access. Due to the high number of possibilities, they are not included in the current model. We just assume signal characteristics similar to GPS signals, where the measurement noise can be adjusted according to the mission design interests.

The ground segment module carries out the POD in the postprocessing mode and produce outputs similar to the receiver independent exchange (RINEX) file format, containing measurements taken by GNSS receivers onboard the simulated LEO satellites. Then, an ephemeris model is generated for the users, which can be broadcast by Internet protocol as we deal with postprocessing mode. It should be noted that LEO satellites can be equipped with GNSS receivers to perform orbit determination directly within the space segment. This capability reduces potential issues associated with data transmission failures and the limited availability of ground stations within the satellite's footprint. By conducting orbit determination in the space segment, the overall system autonomy can be enhanced. However, it is important to acknowledge that real-time POD is currently not feasible for several reasons. These reasons include constraints such as limited onboard CPU and power resources, the sensitivity of sensors to noise, and the requirement for accurate orbits and clocks in space. Nevertheless, advancements in technology may address these challenges in the future, particularly with the advent of new generations of GNSS corrections provided by initiatives such as the Australian SouthPAN, Japanese MADOCA, and European Galileo HAS [41], [42]. In this manner, we currently assign the responsibility of POD to the ground segment, where it is traditionally performed. Nevertheless, we recognize the importance of exploring the possibility of conducting POD directly within the space segment in real-time applications.

In the user segment module, the GNSS measurements are simulated as received in ground receivers, including pseudoranges (P), carrier phases (L), Doppler shifts (D), and instrumental noises. These measurements are then used to perform Doppler-based positioning or PPP.

In total, nine modules define the end-to-end LEO-S9 process, allowing to apply positioning techniques with signals of opportunity (SoO) [30], [43], [44], with dedicated signals using independent navigation systems [45], or with LEO satellites augmented by the GNSS [11], [46]. The next sections show the details of each of the model segments: space segment (see Section III), signal propagation (see Section IV), ground segment (see Section V), and a user segment (see Section VI).

III. SPACE SEGMENT

The main elements of interest in the space segment module are: 1) the constellation design and 2) the instruments carried by each satellite, such as antenna, clocks, and GNSS receivers. Section III-A presents the simulation of LEOs. The remaining sections present the relevant instruments and parameters related to the components that affect the overall accuracy of the system, i.e., the GNSS payload and the navigation payload. The supporting parts of the satellite, which provide the structure, power, commands for satellite operation, telemetry, appropriate thermal environment, radiation shielding, and attitude control are out of the scope of the simulations.

TABLE II
Keplerian Orbital Parameters

e	Eccentricity
i	Inclination
A	Semi-major axis
ω	Argument of periapsis
Ω	Right ascension of ascending node
M_0	Mean anomaly

A. Constellation Design

An intuitive way to initialize the LEO is using the Keplerian orbital parameters. The six orbital elements, described in Table II, specify the orbit eccentricity, inclination, altitude, and the starting point of the orbit at a particular time. Details on how to use them in orbit determination are shown in [14] and [47]. The Keplerian orbital parameters allow us to initialize the satellite orbits. A realistic scenario, therefore, must also include an orbit propagator to govern the satellite motion over time. To this end, the constellation is simulated using the Cowell numerical integration [48], including the earth's gravity, J2 perturbation due to the earth's shape, third body effects, solar radiation, and atmospheric drags. The impact of these perturbation effects in LEO satellite orbits is discussed in [15], [49], [50], [51], and [52]. All of these effects are incorporated in our simulations based on the poliastro tool [53], an open-source Python library.

The simulation of a LEO-PNT system should be capable of, at a minimum, reproducing the LEO constellations with a Walker delta topology, which allows near-circular satellite orbits that keep a symmetric coverage by the user in the ground [54], [55], [56]. To this end, the developed simulation allows us to deploy evenly distributed planes over a full 360° reference plan. The input values are the number of planes, number of satellites per plane, orbit inclination, altitude, and eccentricity. The argument of periapsis is fixed in all the experiments. The right ascension and mean anomaly, on the other hand, are defined to evenly distribute the satellites within the constellation and keep the Walker delta topology.

To define reasonable values of the orbit inclination, altitude, and eccentricity, our investigation is carried out using the geometric dilution of precision (GDOP) computed for range-based positioning as a basis. Fig. 2 shows four types of satellite coverage (left panels) and expected precision (right panels) when varying the orbit inclinations. We have simulated 441 satellites distributed in three constellations with the following inclination angles: 85°, covering mainly the polar region; 55°, covering mostly the mid-latitudes; and 25°, covering the low-latitudes. When a unique orbit inclination is used, the constellation covers mainly a specific region. One can notice that the highest inclination can provide up to 54 satellites in view, while lower inclinations provide 22–24 satellites in view. In polar orbits, the number of satellites in view is concentrated in the small part of the polar regions, while lower inclinations generate more balanced distribution worldwide. In addition,

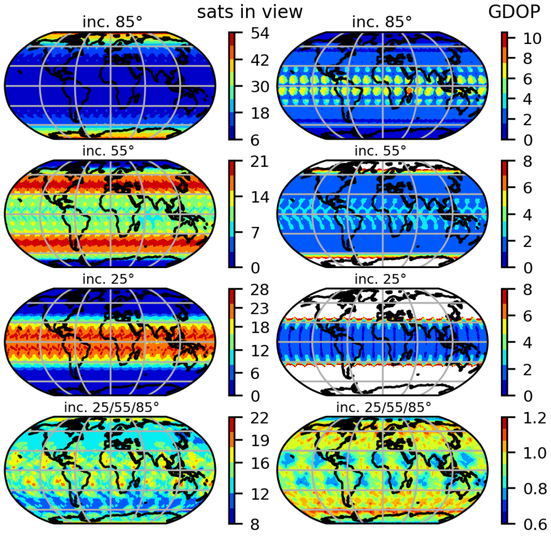

Fig. 2. Relation between the orbit inclination, number of satellites in view, and GDOP for range-based positioning. LEO-S9 simulations are performed to obtain constellations with three orbit inclinations: 85°, 55°, and 25°. Bottom panels are derived from merging the three orbit inclination planes. All the cases are developed using a fixed number of 441 satellites.

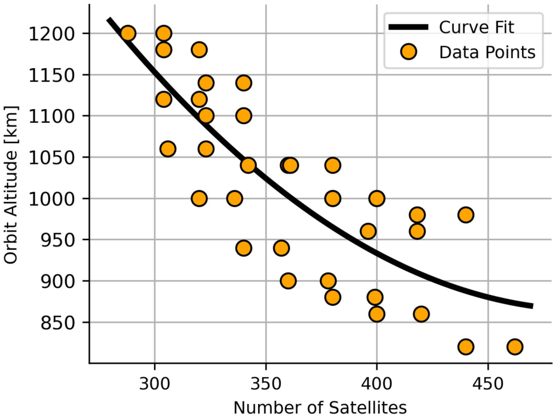

Fig. 3. Relation between the orbit altitude and the minimum number of satellites to have a maximum GDOP value lower than 4. The LEO constellation was simulated with three orbital planes of inclination angles equal to 85°, 55°, and 25°.

an evenly distributed constellation is obtained when the three inclination planes are merged (bottom panels). By merging these three inclination planes, we can obtain a minimum of eight satellites in view globally. In addition, it allows a GDOP [57] value of below 2 in global scale, which is excellent for positioning. These results strongly indicate that merging three orbit inclination planes can optimize the entire LEO constellation for PNT applications, as also discussed in [6], which has motivated us to define this configuration as default in the LEO-S9 model.

The orbit altitude is another relevant parameter for the system coverage and GDOP. To define an optimized value for our simulations, Fig. 3 shows a relation of the orbit altitude and the required number of satellites to keep the GDOP values below 4 in global scale. From this example, around 450 satellites are required for a constellation with 800-km altitude. As the satellite constellation is placed in higher orbits, the system coverage increases, and the required number of satellites decreases. At 1000 km, for instance, the required number of satellites is ∼25% lower to provide an excellent geometry for positioning. The tradeoff, however, is that signal path losses increase with the increase in altitude. For the simulations, we have used an orbit altitude of 800 km with 441 satellites, which allowed to keep the GDOP$<$4.

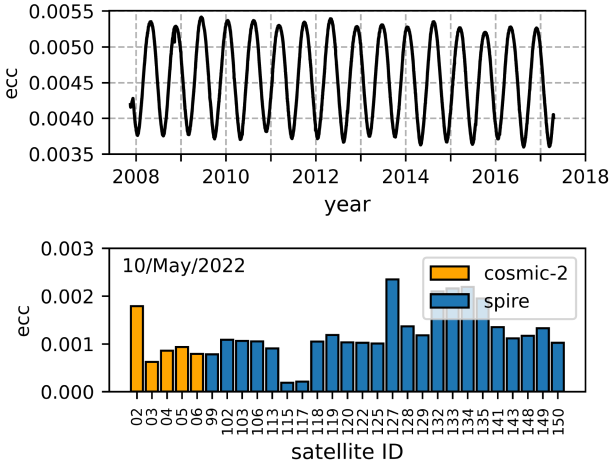

Fig. 4. Eccentricity values from the entire lifetime of satellite C001 of the COSMIC-1 mission (top panel) and from 29 satellites used in the COSMIC-2 and SPIRE missions.

Once defined the orbital inclination and altitude, a missing information to develop the simulations is the eccentricity. In this regard, a dedicated study is presented in Fig. 4 to define reasonable eccentricity values for LEO satellites. The eccentricity values in the top panel are derived from the entire lifetime of the satellite C001 of the FORMOSAT-3/COSMIC mission (COSMIC-1 in short), which is flying at 800 km with an inclination of 72°. The bottom panel shows eccentricity values computed for 29 LEO satellites on May 10, 2022, derived from the constellations of the FORMOSAT-7/COSMIC-2 [58] and Spire Global Inc. [59] missions. From this analysis, we could observe a reasonable interval of the eccentricity values between 0.001 and 0.006. It is worthy to mention that we have not found high correlations between the eccentricities and the inclination angles. We have also not observed correlations between eccentricities and orbit altitudes, where the satellite altitudes are ranging from 470 up to 850 km and the inclinations are varying from 24° to 82°. The future simulations are, then, performed with an intermediate value of 0.003 for all inclination planes and altitudes.

B. Onboard Clocks

Onboard clocks are used in the GNSS payload and navigation payload. The GNSS payload is equipped with instruments designed for orbit determination, while the navigation payload assumes the responsibility of generating and transmitting signals specifically dedicated to PNT. To represent the clocks in both payloads, we have adopted a

TABLE III
Adopted Values for the Clock Simulations

Clock Term	Values
Offset	$-1.00 < a_0 < 1.00$ ms
Drift	$-0.05 < a_1 < 0.05$ ns/s
Drift rate	$a_2 = 0.00$ ns/s^2
Crystal clock stability	$\sigma_\tau = 10^{-11}$ (1s)
Atomic clock stability	$\sigma_\tau = 10^{-12}$ (1s)

The minimum and maximum clock offsets, drifts, and drift rates were derived by the GPS broadcast messages from 1995 to 2020.

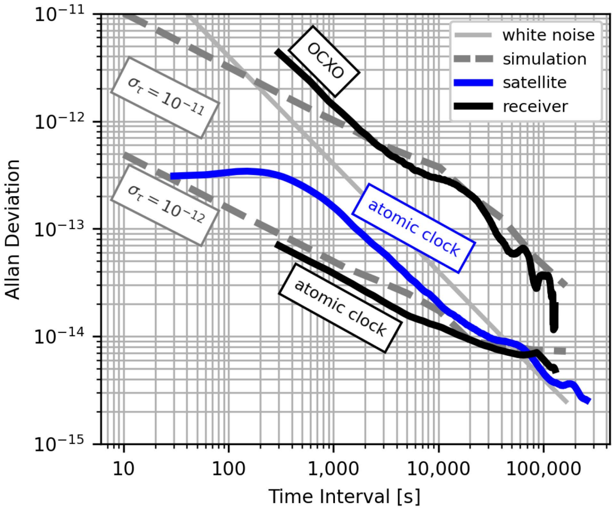

Fig. 5. Allan deviation distributions of atomic and crystal clocks of GPS satellites and receivers. Gray lines refer to simulations using random-walk (dashed) and Gaussian (solid) noise distributions. GPS clocks were obtained by the IGS products.

similar model used in broadcast GPS clocks [60], but with an additional stability term that can vary depending on the simulation requirements, as follows:

$$\delta t^{\mathrm{LEO}} = a_0 + a_1(t - t_0) + a_2(t - t_0)^2 + \psi(\sigma_\tau) \quad (1)$$

where a_0 is the clock offset, a_1 is the clock drift, a_2 is the clock drift rate, and $\psi(\sigma_\tau)$ is a random noise process that depends on the clock stability σ_τ.

The values adopted for the clock simulations are based on the intervals shown in Table III. The clock offset, drift, and drift rate were derived from a large dataset of clock values of the GPS broadcast messages from 1995 to 2020. The shown intervals in Table III refer to the minimum and maximum values obtained from the large GPS dataset. It should be noted that the observed value of zero in all drift rate values of the broadcast products led to the assumption that the drift rate is zero. The stability terms were derived by experimental data and Allan variance [61] analysis. Fig. 5 shows Allan variance values obtained by: 1) oven-controlled crystal oscillators (OCXO), which are clocks used in a typical geodetic-grade GPS receiver; 2) atomic clocks used in GPS receivers; and 3) atomic clocks used in the GPS satellites. The simulated clocks with an Allan deviation of 10^{-11} at $\tau = 1$ s was found close to experimental OCXO clocks. This is depicted by the top gray dashed line, which closely aligns with the black solid line representing the OCXO clock. Atomic clocks, on the other hand, were better represented by Allan deviations of 10^{-12} at $\tau = 1$ s, represented by the close alignment between the bottom gray dashed line and the black and blue solid lines. These distributions agree with clocks obtained by GNSS-induced errors [61], which reproduces clocks in IGS products.

In Fig. 5, we can observe that the Allan deviation of the experimental clocks is higher at lower τ values, which occurs due to the high impact of noise in the short-term variations. The Allan deviation is lower for the long-term variations, since the noise averages out. To represent such experimental distribution, the simulation model incorporates a random-walk frequency noise to represent $\psi(\sigma_\tau)$, neglecting possible sudden changes (i.e., "jumps") in the clock. An example of the simulated Allan deviations using two stability terms with random-walk distributions is incorporated into Fig. 5 (dashed gray lines). As presented, the simulated Allan deviations show that the random-walk noise distribution is compatible with the expected nonstationary noise processes from GPS clocks. We also include a distribution considering the clock noise as a white Gaussian process to exemplify how far the simulation can be from a realistic scenario in case the noise is not properly considered.

In LEO-PNT systems, the accuracy of clock simulations is influenced by additional sources of error, including the residual errors of POD models, the complex space environment, temperature variations, and the internal heat transfer between different components [62]. Employing postprocessing POD solutions and a temperature control system can effectively mitigate these errors. However, in addition to the model provided in (1), it is crucial to incorporate the accuracy of the POD model into the simulation. In the real setup of the Luojia-1A satellite, a frequency accuracy at the level of tens of nanoseconds was achieved [1] when the clocks were synchronized using GPS/Beidou signals. Our simulation setup replicates a similar environment, allowing us to observe clock instabilities that introduce a carrier phase measurement noise of approximately 1.8 cm. More details on the achieved accuracy are shown in Sections V and VI.

In addition to the natural presence of noises and instabilities, clocks on the receiver and the transmitter experience different relativistic frequency shifts, i.e., the frequency ticks by the transmitter differ from those of a clock in the receiver due to relativistic effects. To consider the relativistic effects, the following equation is incorporated in the simulations [63]:

$$\Delta_{\mathrm{rel}} = -2(\mathbf{r} \cdot \mathbf{v})/c^2 \quad (2)$$

where **r** and **v** are the position and velocity vectors of the transmitter, respectively.

C. GNSS Payload

The GNSS payload incorporates all the instruments required for POD based on GNSS. To this end, we adopt GNSS receivers as the main instruments to drive the satellite POD. Together with the GNSS receiver, the GNSS payload also includes a GNSS antenna and an attitude determination and control system (ADCS). Based on these instruments, the main parameters to perform the simulations are considered as the receiver clock, antenna parameters (PCO and PCV), instrumental biases, and measurement noises. In our simulation, we assume that the ADCS is effective in maintaining the antennas pointing toward the earth and the solar cells oriented toward the Sun. We, therefore, assume that there is adequate control over external disturbances, including gravity-gradient torque, aerodynamic torque, solar radiation torque, and earth magnetic torque. This enables the satellite to maintain a fixed orientation relative to its orbit and ensures a stable attitude. Nevertheless, we do not replicate the periodic satellite maneuvers performed by satellite operators.

The PCO and PCV are obtained from the antenna exchange format (ANTEX) file from IGS. We consider a typical TRM59800 antenna to extract such parameters. For the clocks, the simulation is based on the equations presented in Section III-B, considering two options: OCXO and atomic clocks. To simulate the instrumental noises (ϵ), we have adopted the same precision as geodetic-grade GPS receivers. In this sense, GPS pseudoranges are considered 100 times noisier than the carrier phase measurements and a white Gaussian distribution is used [64], [65]. Like common positioning tools, such as RTKlib [66], the standard deviation of 3 mm is adopted as the default option for the raw phase measurements, leading to 30-cm standard deviation in the code measurements.

In case of the instrumental bias, we cannot access experimental values in its absolute form. On the contrary, the instrumental biases have only been observed in relative terms. Several previous studies have considered distinct frequencies, stations, satellite missions, and chipping rates to analyze the DCB. All of them have observed DCB values in the level of nanoseconds (see, e.g., [67], [68], and [69]), so our simulations also assume the magnitude of the absolute bias as nanoseconds. The developed model primarily focuses on simulating the interfrequency biases, specifically assuming satellites from the same mission and utilizing a single modulation type. For this reason, the model does not account for intersystem bias [70]. The instrumental bias is randomly created with a certain nanosecond interval for each satellite, frequency, and receiver. To quantify a reasonable interval, Fig. 6 presents a long time series of the DCB values produced by the center for orbit determination in Europe (CODE) from several satellites and receiver stations. From such analysis, we have defined a reasonable interval of −30 to 60 ns for the instrumental biases. In addition, as IGS, we are imposing the sum of the interfrequency DCB values equals to zero [71], [72].

D. Navigation Payload

The navigation payload consists on the mission data unit, which typically transmit RF signals and frequency standards to the users. The three main parts of the navigation payload consists of the processor/baseband, RF equipment, and frequency standards. Our simulator does not deal with the processor/baseband, so the generation of pseudorandom codes and their modulation with digital data are not reproduced. Nevertheless, DCBs generated by the transmitting instruments are simulated with the same strategy presented in Section III-C.

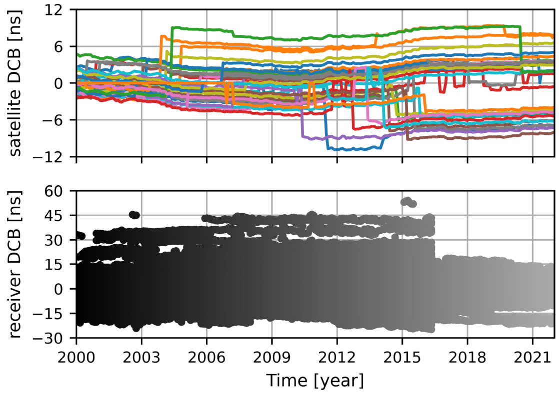

Fig. 6. Long time series of DCB (P1–P2) values derived from the CODE products.

Regarding the RF equipment, the developed model mainly reproduces the transmitting antenna onboard the LEO satellites. The transmitting antenna type may vary depending on the chosen frequency. Larger antenna types, such as wire, patch, and slot antennas, are required for low carrier frequencies (very high frequency, ultrahigh frequency, *L*-band, and *S*-band). At higher frequency (*Ku*-band, and *K*/*Ka*-band), reflectors and reflect-array antennas are more used. Due to the large number of antenna options, the LEO-S9 model does not currently deal with all the options of antenna patterns and gains. The main parameter to be adjusted in the simulations is the frequency, influencing the atmospheric delay of the reproduced observations. We assume that our simulations mainly deal with *S*-bands or lower. In case higher frequencies are used, the geostationary earth orbit (GEO) forbidden region needs to be also considered since certain frequency bands, such as *Ku* and *K*/*Ka* bands, cannot be utilized in the restricted areas to avoid interference with GEO satellites, thereby ensuring efficient spectrum sharing and minimizing potential signal degradation [73].

Our simulation is inspired by the CentiSpace mission, currently in development within the frequency bands equivalent to the GPS. While the L1 and L2 frequency bands are typically reserved for the GPS, we have selected them as the default options to establish a baseline for comparison against the GPS. However, in practice, the potential reuse of the L1 and L2 bands depends on ensuring that the LEO-PNT signal does not cause interference with existing GNSS systems. Given the frequency of interest, all consequent computations are performed neglecting the antenna size dimensions and type. The antenna calibration parameters PCO and PCV vary from frequency to frequency and can produce an error of a few meters if neglected. As default, we are adopting the PCO and PCV values from the GPS satellite PRN-01 of BLOCK IIF. These values are obtained from the ANTEX file from IGS.

The frequency standard, given by the onboard clocks, is the heart of the navigation payload. The atomic clocks used nowadays as references for PNT applications are made by passive hydrogen maser and rubidium atomic frequency standards, which are too large and consume too much power for use in small LEO payloads. However, our simulations are performed considering atomic clocks as precise as the GPS atomic clocks. This assumption is grounded in the fact that time synchronization in LEO satellites can be improved by using onboard GNSS receivers [74]. Hence, the clock model presented in Section III-B can be employed.

IV. SIGNAL PROPAGATION EFFECTS

Various effects can produce signal refraction, reflection, loss, diffraction, and polarization shifts. The current simulation deals with effects that can be seen as delays in the PNT observations, since they have a severe impact in the overall accuracy of the LEO-PNT system. The module of signal propagation aims to reproduce the delay effects over the pseudorange, carrier phase, and Doppler-shift measurements. The following equations present typical representations used in the GNSS of the pseudorange P (3) in meters, carrier phase ϕ (4) in meters, and Doppler shifts D (5) in m/s:

$$P = c\Delta t = \rho + c\left(\delta t^{r} - \delta t^{s}\right) + I + T + m + \epsilon_P \tag{3}$$

$$\phi = \rho + c\left(\delta t^{r} - \delta t^{s}\right) - I + T + m + B + \Phi_r^s + \epsilon_\phi \tag{4}$$

$$D = \left(\dot{\mathbf{r}}_s^T - \dot{\mathbf{r}}_r^T\right)\frac{(\mathbf{r}_r - \mathbf{r}_s)}{\rho} + c\left(\delta\dot{t}_r - \delta\dot{t}_s\right) + \dot{I} + \dot{T} + \epsilon_D \tag{5}$$

where c is the speed of the light, ρ is a geometric distance between the transmitter and the receiver, δt^r and δt^s are the receiver and satellite clock errors with respect to a time system, respectively, I is the ionospheric delay, T is the tropospheric delay, and m is the delay caused by multipath. Terms ϵ_P, ϵ_ϕ, and ϵ_D indicate the thermal and instrumental noises of the pseudorange, carrier phase, and Doppler shift, respectively, including receiver and satellite instrumental delays and satellite orbit errors. The term B stands for the bias term referred to the first tracking instance and Φ_r^s is the term accounting for antenna phase center offset and variations in the receiver and transmitter. Terms $\mathbf{r}_r$ and $\mathbf{r}_s$ are the 3-D coordinate position vectors of the receiver and satellite tied to the signal reception time, respectively, $\dot{\mathbf{r}}_s$ and $\dot{\mathbf{r}}_r$ are the velocity vector of the satellite and receiver, $\delta\dot{t}_r$ and $\delta\dot{t}_s$ are the clock bias drifts, $\dot{I}$ is the ionospheric delay rate, and $\dot{T}$ is the tropospheric delay rate.

The following sections present the effects that need to be modeled when simulating the pseudorange, carrier phase and Doppler-shift observable with a reasonable level of accuracy. Details are presented to demonstrate how to consider the earth's rotation, phase windup, relativistic path range, ionosphere, and troposphere. Additional analyses are presented to quantify the expected impact of such errors in the upcoming LEO-PNT systems.

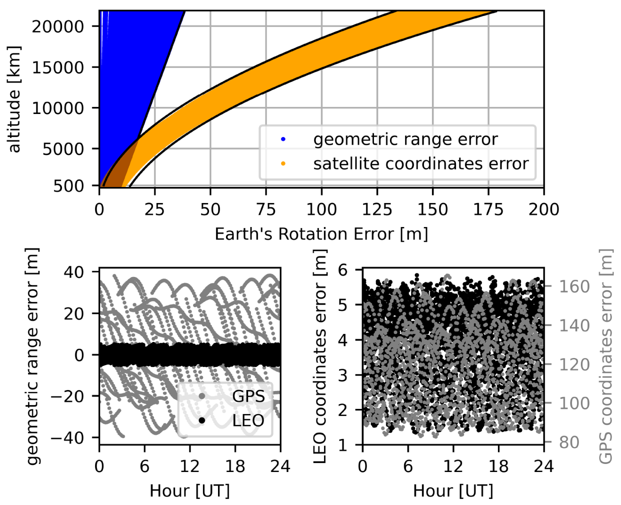

Fig. 7. Impact of the earth's rotation effect on the coordinates of GPS and LEO satellites. The top panel shows a simulation of the earth's rotation impact over satellites placed in distinct altitudes. Bottom panels show the magnitude of the earth's rotation effect when using real GPS satellites and simulated LEOs at 800 km. The results are referred to DOY 6, 2021. The geometric range error refers to the direct impact of the earth's rotation in the range (ρ) measurements. The satellite coordinates refer to the error of the satellite 3-D coordinates in case the rotation is not applied.

A. Earth's Rotation

A precise simulation of the carrier phase, pseudorange, and Doppler shift must include the earth's rotation effect: a relative error known as the Sagnac effect [75]. During the signal propagation time Δt, the earth's coordinate system rotates, requiring a correction to tie all measurements to the coordinate system of the reception time. The correction of the earth's rotation is obtained by rotating the coordinates of the transmitting antenna by an angle $\alpha = \omega_E \Delta t$ over the z-axis. The equation to consider the earth's rotation is given by

$$\mathbf{r}_s = \mathbf{R}_z(\omega_E \Delta t)\mathbf{r}_{s,\text{emission}} \tag{6}$$

where ω_E is the angular velocity of the earth, $\mathbf{R}_z$ is a rotation matrix over the z-axis, and $\mathbf{r}_{s,\text{emission}}$ is the satellite coordinate vector tied to the signal emission time.

To quantify the earth's rotation effect, Fig. 7 (top panel) shows a simulation of the earth's rotation impact over satellites placed in distinct altitudes. The geometric range error refers to the direct impact of the earth's rotation in the range (ρ) measurements. The satellite coordinates refer to the error of the satellite 3-D coordinates in case the rotation is not applied. As we can see, both error types increase with the altitude, being the satellite coordinates more severely impacted and reaching up to 175 m in the MEO altitudes. At lower altitudes, both geometric ranges and satellite coordinate errors severely reduces. Fig. 7 (bottom panel) shows an example of the magnitude of the earth's rotation when using real GPS satellites and simulated LEOs at 800 km. Whereas the GPS coordinates are affected up to 40 m (range) and 160 m (coordinates), LEO satellites at 800 km are impacted by around 6 m. Indeed, the impact of the earth's rotation in LEO satellites is reduced once the expected propagation time Δt is lower in comparison to MEO satellites. It is shown that the impact of the earth rotation reduces by approximately 75–97% for LEO satellites related to the geometric range and 3-D satellite coordinate errors, respectively.

B. Phase Windup

As the satellite moves along its orbit, the platform continuously rotates to keep the solar panels pointed in the direction of the sun for maximum exploitation of the solar energy. The antenna rotation on the transmitting platform causes a phase variation in the circularly polarized waves. This phase variation, known as a phase windup, provide range accumulation in the counting number of cycles used to generate the carrier phase measurements. It can be written as [76], [77], [78]

$$\Delta\Phi = 2N\pi + \Delta\phi \tag{7}$$

where

$$\Delta\phi = \text{sign}(\xi)\cos^{-1}\left(\frac{\mathbf{D}'\cdot\mathbf{D}}{||\mathbf{D}'||\cdot||\mathbf{D}||}\right) \tag{8}$$

$$N = \text{int}[(\Delta\Phi_{\text{i}-1} - \Delta\phi_{\text{i}})/2\pi] \tag{9}$$

$$\xi = \mathbf{k}\cdot\left(\mathbf{D}'\times\mathbf{D}\right) \tag{10}$$

$$\mathbf{D} = \mathbf{x} - \mathbf{k}(\mathbf{k}\cdot\mathbf{x}) + \mathbf{k}\times\mathbf{y} \tag{11}$$

$$\mathbf{D}' = \mathbf{x}' - \mathbf{k}\left(\mathbf{k}\cdot\mathbf{x}'\right) + \mathbf{k}\times\mathbf{y}' \tag{12}$$

where $\mathbf{x}$, $\mathbf{y}$, and $\mathbf{x}'$, $\mathbf{y}'$ are the dipole unit vectors of the transmitting and receiver antennas, respectively, $\mathbf{k}$ is the unit vector from the satellite to the receiver, and i is the epoch time. The operators sign and int return the sign and integer value of a real number, respectively.

The apparent range increases because the phase windup depends on the transmitted frequency and the platform rotation speed. Usually, the phase windup in classic GNSS systems varies slowly with time; however, faster panel rotations are expected in LEO satellites due to the higher orbital speed. To demonstrate typical values of phase windup computed by LEO and classic GNSS satellites, Fig. 8 shows a simulated example only considering rotations in the satellite platforms. The top panel shows the range accumulation due to the phase windup considering an elevation cutoff angle of 0°. The bottom panel shows the nonaccumulated part of the phase windup ($\Delta\phi$) without any elevation mask. As can be seen, the LEO satellites provide much shorter arcs (top panel). Any misrepresentation of the phase windup will, therefore, provide a lower impact on the ambiguity estimation. On the other hand, the number of platform rotations is much higher for LEO satellites (bottom panel). While the GPS platform rotates twice per day, seen by two $\Delta\phi$ peaks, the LEO satellites at 800 km perform 14 full rotations, related to the orbital revolutions.

C. Relativistic Path Range

Due to the curvature produced by the gravitational field, a general relativistic correction to the geometric range is essential for subcentimeter representation of the pseudorange and phase measurements. The relativistic effect on the path range, also known as Shapiro signal propagation delay, is described by the following expression [63]:

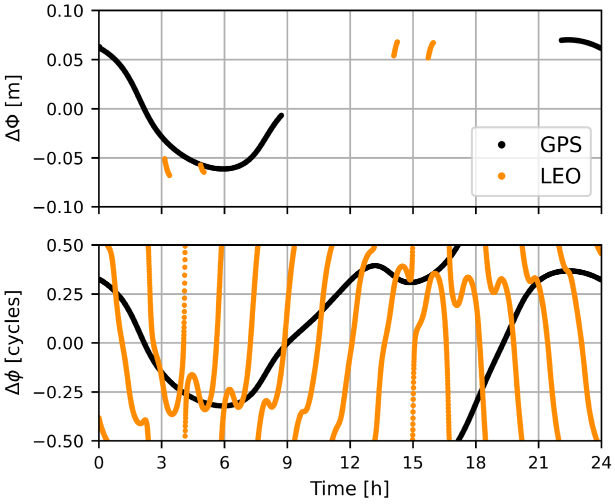

Fig. 8. Examples of accumulated ($\Delta\Phi$) and partial ($\Delta\phi$) phase windup. A cutoff angle of 0° was used in the top panel. No cutoff angle was used in the bottom panel. The GPS satellite is referred to PRN 1 in DOY 6, 2020. The LEO satellite is simulated at an altitude of 800 km. All the simulations were conducted using the L1 frequency as a base.

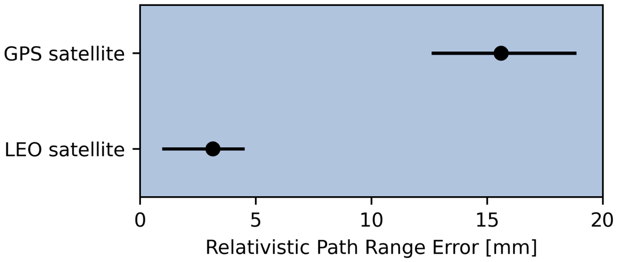

Fig. 9. Error interval due to the relativistic path range for GPS and LEO satellites. GPS data were obtained by precise IGS files. LEO data were obtained by the developed simulation model. The example is referred to DOY 6, 2021.

$$\Delta\rho_{\text{rel}} = \frac{2\mu}{c^2}\ln\frac{||\mathbf{r}_s|| + ||\mathbf{r}_r|| + \rho}{||\mathbf{r}_s|| + ||\mathbf{r}_r|| - \rho} \tag{13}$$

where $||\mathbf{r}_s||$ and $||\mathbf{r}_r||$ are the norm of satellite and receiver coordinates, respectively, ρ is the geometric distance, and μ is the gravitational parameter.

The magnitude of the relativistic effect on the GPS path range with a ground receiver is well represented by the example shown in Fig. 9. This figure also presents the expected relativistic impact on LEO-based navigation systems with satellites placed at 800 km. As can be seen, the range delay $\Delta\rho_{\text{rel}}$ using GPS satellites is around 13–19 mm. In LEO heights, the magnitude much reduced, lying around 1–4 mm. Therefore, any misrepresentation of this effect will reduce the modeling errors in future LEO-PNT missions.

D. Ionosphere

Several empirical models have been developed over the last few decades to describe the total electron content

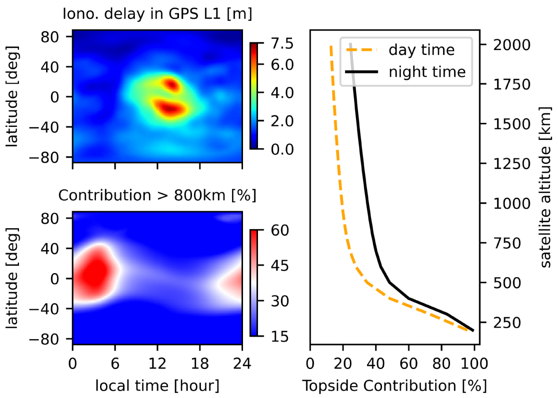

Fig. 10. Top-left panel shows a global distribution of the ionospheric delay in meters at the L1 GPS frequency obtained from ground to GNSS orbit height. The bottom-left panel shows the corresponding ionospheric delay contribution from the plasmasphere and topside ionosphere in %, considering a LEO satellite at 800 km. The right panel shows average values of the ionospheric contribution above LEO satellites placed at several altitudes. The example corresponds to DOY 6, 2021, at 12 h UT (Universal Time).

(TEC) and correct the ionospheric delay in the GNSS observations. Most of the ionospheric models rely on 2-D representations of the ionosphere, such as the Klobuchar model [79], BeiDou global broadcast ionospheric delay correction model [80], and the global ionospheric maps (GIMs) provided by IGS [81]. They can be efficiently used to represent the ionospheric delay in the signal path between the classic GNSS satellites and the ground. However, in LEO-PNT, a large region above the LEO height (up to 20 000 km), corresponding to the topside ionosphere and plasmasphere [82], [83], [84], should be removed from the current ionospheric models. In this regard, 3-D models are more realistic for LEO-PNT systems.

To account for the requirements of the upcoming LEO-PNT systems, the developed simulation model uses a similar approach to the method developed by Prol et al. [85] to estimate the 3-D ionospheric/plasmaspheric model. In [85], the global-scale tomography was performed using around 2700 GNSS stations, requiring high processing time. To reduce the computational burden of the 3-D estimations and allow us to generate simulations with a reasonable processing time, the LEO-S9 model is developed only using vertical TEC (VTEC) observations. The VTEC observations are obtained from the GIMs developed by the CODE. The VTEC values are then inverted into 3-D electron densities by data ingestion. An evaluation of the proposed ionospheric model is shown in Sections V and VI.

To quantify the expected impact of the ionosphere/plasmasphere in LEO systems using the developed model, Fig. 10 presents the estimated ionospheric delays using LEO in comparison to typical values in the GNSS. The top-left panel shows a global distribution of the ionospheric delay at the L1 GPS frequency obtained from ground to GNSS receivers. The corresponding topside contribution is shown in the bottom-left panel, considering the LEO satellite flying at 800 km. The right panel shows average values of the percentage contribution for distinct scenarios of LEO satellite altitudes. Overall, we can observe contributions of around 15–60%, depending on the latitude, local time, and satellite altitude. The highest contributions occur in the nighttime, low-latitude regions, and at lower LEO heights. Therefore, the lower altitudes at which LEO satellites are positioned, specifically at 800 km, result in reduced errors introduced by the ionosphere, ranging from approximately 40% to 85% in the LEO-PNT measurements. If the LEO satellite is placed below 500 km, the error contribution sharply decreases, reaching almost 0% at 250 km.

E. Troposphere

The troposphere extends from the ground up to lower altitudes than LEO satellites. Identical empirical models used in classic GNSS can, therefore, be used in LEO-based navigation systems. Our simulations are performed using the troposphere model recommended for GNSS augmentation systems, named RTCA MOPS model [86], [87]. The RTCA MOPS model is based on meteorological data of air pressure, temperature, water vapor pressure, temperature lapse rate, and vapor pressure. The meteorological values are derived by the U.S. standard atmosphere supplements and organized in the form of a table. Therefore, the model does not require external information about the actual state of the atmosphere.

The two main parameters estimated by RTCA MOPS are the zenith hydrostatic delay (ZHD) and zenith wet delay (ZWD). At the mean sea level, they are defined as

$$\mathrm{ZHD}_0 = 10^{-6} k_1 \frac{R_d p}{g_m} \tag{14}$$

and

$$\mathrm{ZWD}_0 = 10^{-6} k_3 \frac{R_d}{g_m(\lambda + 1) - \alpha R_d} \frac{e}{T} \tag{15}$$

where k_1 is the refraction coefficient for dry air, R_d is the constant of dry air, g_m is the mean gravity, p is the pressure of air at mean sea level, k_3 is a refraction coefficient for wet air, e is the water vapor pressure at mean sea level, λ is the vapor pressure decrease factor, α is the temperature lapse rate, and T is the temperature at mean sea level. More details about these parameters are shown in [88].

After computing the tropospheric delays at the mean sea level (ZHD_0 and ZWD_0), a reduction to the receiver height (H) is required. The following formulas are applied to reduce tropospheric delay above the mean sea level:

$$\mathrm{ZHD} = \left(1 - \frac{\alpha . H}{T}\right)^{\frac{g}{R_d \alpha}} \mathrm{ZHD}_0 \tag{16}$$

$$\mathrm{ZWD} = \left(1 - \frac{\alpha . H}{T}\right)^{\frac{(\lambda+1) g}{R_d \alpha} - 1} \mathrm{ZWD}_0 \tag{17}$$

where g is the gravity acceleration.

Once the troposphere is equal in both LEO and MEO systems, there is no necessity to demonstrate how the RTCA MOPS model applied in the classical GNSS would differ to LEO-based navigation. We, therefore, show in Fig. 11 the expected accuracy of the RTCA MOPS model in both the

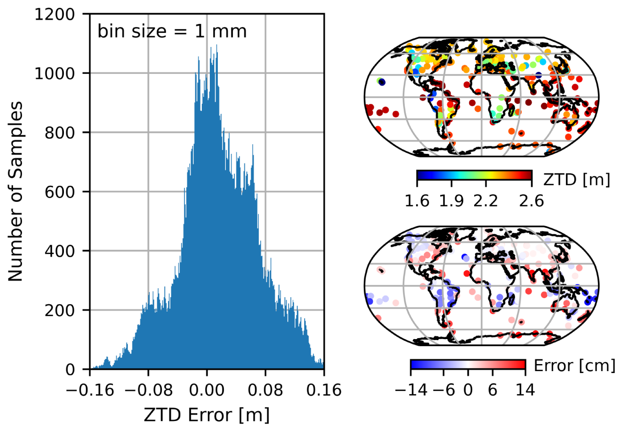

Fig. 11. Tropospheric delay accuracy of the RTCA MOPS model. Reference values were obtained by the IGS final products of the troposphere. The example corresponds to DOY 6, 2021. The left panel shows an histogram of the error considering the entire day of data. The right side panels show the estimated ZTD and the corresponding error for 0 h UT.

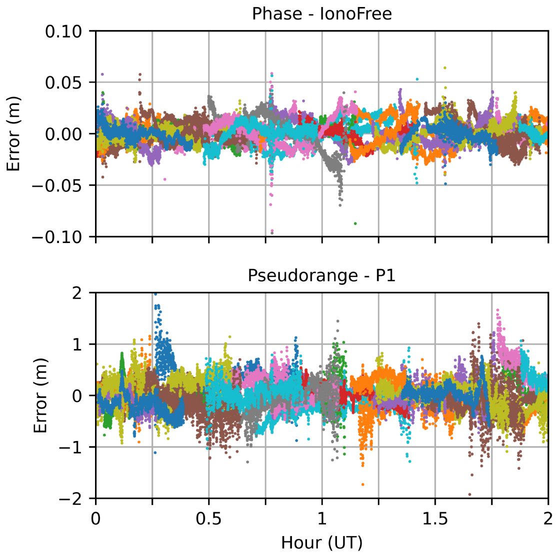

Fig. 12. Accuracy evaluation of the phase and pseudorange simulations of the LEO-S9 model in comparison to real measurements obtained by the GPS receiver onboard SWARM. The top panel refers to the ionospheric free linear combination. The bottom panel shows the undifferenced P1 observations. Each color represents a different GPS satellite. The example is performed in DOY 6, 2021.

systems. The evaluation is presented in terms of zenith total delay (ZTD = ZHD + ZWD) considering several GNSS receiver stations during DOY 6, 2021. The worldwide distribution of the stations is presented in the right panels. The reference ZTD values were obtained by the IGS final products of the troposphere. As can be seen, the expected error lies around ±16 cm with the average of the error centered at zero. No clear bias is observed in the error distribution; however, a slight worse performance is observed in the Southern hemisphere, which is expected since the RTCA table was built with measurements in the Northern hemisphere. Our simulations, therefore, are expected to obtain similar accuracy for zenith delays. An additional error increment, however, is expected since the tropospheric delay computation requires to convert the zenith delay to the slant direction. To this end, the well-known Niell mapping function (NMF) is used. A numerical validation of the NMF is presented by Qiu et al. [89], showing an accuracy higher than 5 cm for elevation angles above 10°.

V. GROUND SEGMENT

The ground segment module is the main responsible for the maintenance of the navigation system. The related tasks for the simulation model in this segment are the generation of the GNSS measurements onboard the LEO satellites and the POD. Therefore, the simulated LEO-PNT system depends on the GNSS for precise positioning and time synchronization. We assume that achieving complete independence is challenging because it requires large atomic clocks that consume a significant amount of power. In addition, the satellite clocks must be cost effective, especially when deploying a practical LEO constellation with numerous satellites. Due to these challenges, particularly associated with size, weight, power, and cost of clocks and navigation payloads, our simulation is not reproducing independent systems. The next sections show how the tasks of the ground segment are performed by the LEO-S9 model, with their corresponding accuracy. The communication links and the specific methods used by the ground segment for system maintenance fall outside the scope of our investigation.

A. Onboard GNSS Measurements

The main GNSS measurements to the ground segment simulations are the carrier phase, pseudorange, and Doppler shifts. The range-based measurements are enough for POD; however, we also include Doppler-shift observations since it can be efficiently used to derive the satellite velocity in further analysis. These observations are obtained through (3)–(5), presented in Section IV. Notice that the tropospheric delay is neglected since we deal with the environment above the LEO heights, which are above the tropopause (around 60 km).

To demonstrate the capabilities of the model to reproduce pseudorange and carrier phase measurements obtained by onboard GNSS receivers, Fig. 12 presents simulated GNSS observations in comparison to real tracked data by the SWARM-A satellite. The unique terms that were not simulated in this example, but rather estimated, are the GNSS receiver clock and phase bias. We were also not capable to obtain Doppler-shift measurements by real GNSS onboard missions, so we rely in the validation using ground-based GNSS data to represent the Doppler shift, as shown in Section VI.

As can be seen, the simulation allows the GNSS measurement reconstruction up to the level of a few centimeters. When simulating the dual-frequency (DF) carrier phase, in the form of ionospheric free observations, a 3-D root-mean-square error (RMSE) of 1 cm (1-sigma) is obtained, with a maximum error of around 10 cm. In case of the pseudorange simulations, a 3-D RMSE of 28 cm (1-sigma) is observed, with a maximum error of 2 m. This result demonstrates how powerful the LEO-S9 model is to reproduce realistic GNSS observations. The remaining errors of the GPS P1 observations are mainly related to the inherent noises of the measurements and the ionospheric delay. Although we have used a high-resolution 3-D ionospheric model, there are still missing specifications in the ionospheric model that require further improvements. Nevertheless, the obtained accuracy can be considered high for single-frequency POD.

B. Precise Orbit Determination

As shown by the extensive literature review provided by Selvan et al. [90], the most common tracking system to obtain POD of LEO satellites nowadays is based on spaceborne GNSS receivers. A clear trend is observed in techniques using least-squares solvers, DF signals, undifferenced (UD) phase and code observations in the postprocessing mode. This procedure has now evolved into a mature technique, with an average POD accuracy lying around 3–10 cm. To keep up with the most recent trends on orbit determination, the POD solution in LEO-S9 is derived based on phase and code UD observations, the postprocessing mode, and the least-squares estimator. It can be understood as a kinematic PPP algorithm, with the following configurations: 1) daily RINEX files with 1-s interval; 2) only GPS constellation; 3) batch solution, so that no forward and backward filters are necessary; 4) cutoff angle of 10°; 5) no tropospheric delay; 6) ionospheric delay based on the 3-D global ionospheric model (details in Section IV-D) in case of single-frequency solutions; 7) ionosphere-free in case of DF solutions; 8) precise GNSS ephemerides (sp3) and satellite clock corrections (5 s) acquired from IGS products; 9) correction of PCO and PCV of antenna obtained through IGS products; 10) phase windup corrections; and 11) no strategy for ambiguity solution. The accuracy of the POD estimation is equal to the accuracy range of the simulated observations. As shown in Fig. 12, the expected accuracy lies around 1–5 cm, in case of DF, and 30–200 cm for single-frequency solutions.

After the POD solution, the satellite orbits need to be transmitted to the user segment. Keplerian ephemeris models are the usual option in MEO satellites [91] since they allow orbit and clock predictions for a few hours. Unlike MEO, the LEO satellites are much closer to the Earth. Consequent gravity and atmospheric drag forces require more complex orbital dynamics. To overcome this issue, our simulations are based on the premise that the responsibility of sending corrections to users lies with the ground segment, following the traditional infrastructure for providing corrections to PPP users. In line with the practices of IGS, we assume that satellite coordinates and clocks are delivered to PPP users in the form of precise files in the postprocessing mode. In MEO satellites, they allow precise orbit interpolation in the level of a few centimeters by an 11-order sliding-window Lagrange interpolation [92]. In the direction of producing a simulation environment capable of accurate LEO satellite positioning, the developed model uses the same sliding-window Lagrange interpolation.

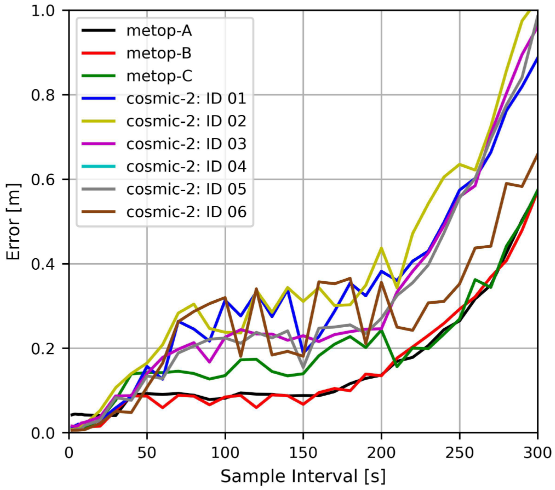

Fig. 13. Error of the sliding-window Lagrange interpolation for several LEO satellite missions. The interpolation was performed considering distinct time steps (or sample rates) to describe the orbit. Only the maximum error during an entire day is shown for each time step. Experimental POD data obtained in DOY 6, 2021 from COSMIC-2 and METOP were used for the validation.

A question still unanswered, however, is the minimum time step required to reproduce a precise LEO interpolation. In the case of classic GNSS, the time resolution to perform the interpolation with IGS products is 15 min. However, this time step is not enough for the accurate interpolation of the LEO satellite coordinates. To define a more realistic time resolution, Fig. 13 shows the error of the sliding-window Lagrange interpolation considering different temporal step sizes of LEOs. We have applied the interpolation over distinct satellite missions and time intervals. In every mission, the POD was performed within a centimetric level by the responsible center, limiting the accuracy of the evaluation. In this analysis, we could observe that a time step of 1 s provides, in maximum, 2 cm of error, while time step sizes of 100 s produce around 20 cm. Consequent simulations that use a time step size of 1 s are, therefore, considerably more reliable. Although the LEO-S9 model can be operated with these distinct time steps, we have defined 1-s time interval for further analysis, which includes a few centimeters of errors (< 2 cm) in the orbit description.

VI. USER SEGMENT

The user segment module comprehends the receivers and antennas that process the measurements and provide solutions for several applications. The overall configuration of the LEO-PNT system gives rise to several possibilities for user segments. Defining the link budget, for instance, requires several assumptions, including the antenna array, power supply, satellite size, solar panel dimensions, clock precision, onboard GNSS receiver, satellite altitude, expected beamforming, signal frequency, ADCS, and signal bandwidth. Incorporating all the necessary requirements for computing the potential gains from

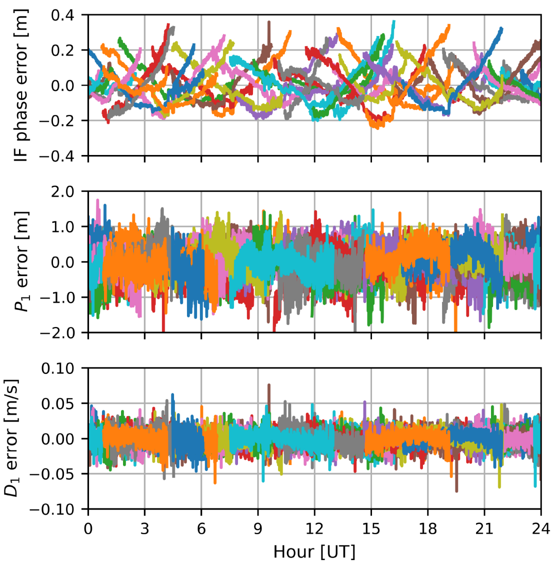

Fig. 14. Accuracy evaluation of the simulations obtained by the LEO-S9 model in comparison to real measurements obtained by the ground GNSS receiver named BRST, in France. The accuracy of the IF phase, P_1 pseudorange, and D_1 Doppler shift is presented in the top, middle, and bottom panel, respectively. Each color represents a different GPS satellite. The example is performed in DOY 6, 2021.

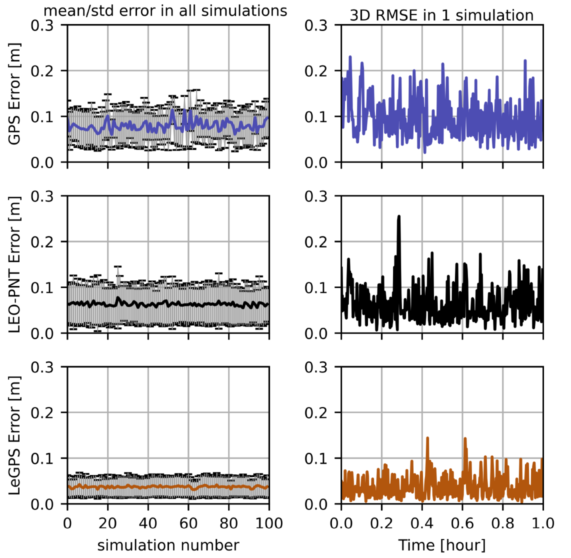

Fig. 15. Range-based positioning error using only GPS data (top panels), only LEO data (middle panel), and GPS augmented by LEO satellites (bottom panels). The LEO constellation is simulated with 441 satellites in three orbit inclinations (85°, 55°, and 25°) at an altitude of 800 km. GPS data are simulated considering the real orbit trajectories in DOY 6, 2021. The receiver is located at 10° × 10° × 200 m in latitude, longitude, and altitude, respectively. A kinematic PPP is performed with a static receiver.

increased signal reception power poses a considerable challenge. Therefore, in this study, we have chosen to focus primarily on the receiver noise level as the main factor driving the user segment performance. As a result, the responsibility for computing the link budget and determining the expected noise level lies with an external party.

The primary objective of this study is to analyze the advantages of LEO systems in terms of geometric gains when compared to the GPS. We have maintained similar signal characteristics to GPS, assuming the availability of a dedicated link budget. Section VI-A shows the accuracy of the LEO-S9 model to reproduce GNSS measurements. Section VI-B shows the expected improvement in positioning domain when including LEO constellations in the PPP estimations.

A. Ground-Based GNSS Measurements

The main measurements of interest to PNT users are the pseudorange, phase, and Doppler shift, described by (3)–(5) in Section IV. Their accuracy, when reproduced by the simulation model, is presented in Fig. 14 for P_1, D_1, and the ionospheric-free carrier phase. These are usual measurements for single-frequency PPP, DF PPP, and PNT based on SoO. It shows a comparison between the simulated GNSS observations and real tracked data by the IGS station named BRST, in France. The receiver clock and phase bias were not simulated in this case but estimated. Overall, the simulated phase RMSE, when compared to real data, is 10 cm, with a maximum of 36 cm. The P_1 RMSE is 44 cm, with a maximum around 2 m. The D_1 RMSE is 1 cm/s, with a maximum of 7.5 cm/s. By this example, the model can be used not only for range-based positioning but also for Doppler-based positioning. A worse performance, however, is observed in comparison to the GNSS measurements shown in Fig. 12 to reproduce POD measurements, mainly in the carrier phase simulations. This is expected since the tropospheric delay plays an important role in the measurement taken on the ground. For instance, we can clearly see a dependence of the phase error with the satellite elevation angle in Fig. 14, which is associated with the misrepresentation of the tropospheric delay estimated by the RTCA MOPS model. Usually, the tropospheric delay is estimated together with the PPP solution; however, we preferred to keep the results obtained by the troposphere model (see Section IV-E) to demonstrate the most realistic accuracy of the simulations. Despite this, LEO-S9 can be considered a powerful model to reproduce GNSS-like signals.

B. Precise Point Positioning

The user positioning simulations were performed using the PPP technique with ionospheric-free observations. The positioning was determined through a kinematic solution, considering the receiver coordinates (X, Y, Z), clock bias, troposphere, and ambiguities as unknown. The coordinates and clocks were considered uncorrelated with time, making the analysis realistic for dynamic users. Fig. 15 (top panel) shows the accuracy level of the range-based positioning reproduced by LEO-S9 when using only GPS observations in the simulations. Middle panels show the solutions based only on LEO satellite. Bottom panels show the results utilizing LEO satellites as a complement to GPS, also known as LEO enhanced GPS (LeGPS). Right panels are the 3-D RMSEs obtained from a single simulation of 1 h.

Left panels refer to the average and standard deviation of 100 simulations. Each simulation is generated with random values of clocks, satellite orbit errors, instrumental biases, and instrumental noises. These values were simulated using realistic intervals and statistic distributions, which are shown in previous sections. In this example, the clocks and orbits are described as precisely as the final products by IGS, so that we can analyze the gains that LEO satellites can provide by just improving the system geometry.

Overall, the simulations using only GPS have provided an average accuracy of 7.9 ± 4 cm (1-sigma), which is a reasonable accuracy in real cases of kinematic PPP with 1-h data collection [93], [94], [95]. The PPP using only LEO data has presented an accuracy of 6.3 ±4 cm (1-sigma). In case of the GPS augmented by LEO satellites, the accuracy improves to 3.7 ± 2 cm (1-sigma). This presents an improvement of 20% when using LEO-based positioning in comparison to GPS-only. In addition, an improvement of 53% is obtained when using LeGPS in comparison to GPS-based positioning, which is mostly related to geometry gains that LEO constellations can offer. However, the main challenge in making this simulated system work in the real world lies in the assumption that it is feasible to implement hundreds of satellites in LEO with similar characteristics to the GPS. While several aspects regarding the feasibility of such a system are still open for discussion, considerable efforts have been underway in recent years to achieve this ambitious goal [4], [5], [6], [9], [11], [56].

VII. CONCLUSION AND FUTURE WORK

This work presented results of a comprehensive simulation of various components of a dedicated LEO-PNT system to PPP. We first introduced which parameters have been adopted to simulate the satellite constellation. Then, we have simulated the most common observations used in satellite-based PNT, such as the pseudorange, carrier phase, and Doppler shift, and discussed the model accuracy to reproduce them. All techniques and parameter intervals adopted to simulate the LEO-PNT system, such as clock model, instrumental noises, code biases, signal propagation models, and PNT strategies, have been defined based on experimental data analysis. This may serve for future developments of LEO-PNT as well as help future simulations. Additional analysis have discussed the differences when using LEO and classic GNSS satellites. The main conclusions of this work regarding the discussions are shown as follows.

1) *Space segment:* We have identified that three orbit inclination planes with around 400 satellites at 800-km height allow excellent worldwide GDOP values with continuous eight satellites in view. LEO-PNT implementations with similar constellation designs are, therefore, recommended in future systems. In addition, atomic and OCXO clocks have found good agreement in comparison to real data when using random-walk distributions and Allan deviations of $10^{-12}(1\,s)$ and $10^{-11}(1\,s)$, respectively, which may serve to future clock simulations.
2) *Signal propagation:* All the considered signal effects (earth's rotation, phase windup, relativistic path range, and ionosphere), despite the troposphere, presented lower impacts in LEO-PNT systems in comparison to classic GNSS. Their impact was 15–97% lower in LEO, depending on the altitude orbit height. So, any mismodeling of the signal propagation effects will influence considerably less in LEO-PNT in comparison to the GNSS.
3) *Ground segment:* Our strategy has demonstrated high accuracy to reproduce the measurements required for POD. An accuracy of 1 cm was obtained to simulate ionosphere-free carrier phase observations retrieved by receiver onboard LEO satellites, with maximum errors of 10 cm. The pseudorange measurements in the L1 frequency were simulated with an accuracy of 28 cm and maximum error of 2 m, which reflects the accuracy of the developed ionospheric model. In addition, we have demonstrated the expected accuracy of the POD ephemeris in LEO satellites. It was considered that the ephemeris coordinates are transmitted to the users in a similar form to the IGS final products. In this analysis, a time step of 1 s has provided a maximum error of 2 cm, while time step sizes of 100 s produced around 20-cm error.
4) *User segment:* In the user segment, the carrier phase ionospheric-free and P1 measurements from ground stations were simulated with lower accuracy than the spaceborne measurements. This is mainly due to the tropospheric delay, which was simulated using the RTCA MOPS model and an NMF. Usually, the tropospheric delay is estimated together with the PPP solution; however, the simulations are limited to the accuracy of the current tropospheric models. The developed model was capable to reproduce Doppler-shift values with errors around 1 cm/s, and maximum errors of 7.5 cm/s. We have also observed that LEO constellations can provide improvements of 20% when using only LEO data and 53% when using GPS augmented by LEO, in comparison to typical GNSS-based PPP solutions with 1 h of data collection.

The simulation presented in this study has shown potential in reproducing accurately the PNT parameters. However, the LEO constellation was simulated with specifications similar to those of GPS satellites operating at lower orbits. While our simulations do incorporate LEO satellites with characteristics similar to GPS satellites, their sizes and specifications will differ. LEO-PNT benefits from the GNSS for precise orbit and clock determination, leading to more feasible requirements for onboard instruments. This allows for notable reductions in clock size, power supply capabilities, and overall satellite dimensions. We acknowledge, however, that our current simulation overlooks the fact that LEO satellite beamforming should be scaled down compared to traditional GNSS systems. This aspect warrants further investigation to ensure a comprehensive understanding of the implications and considerations for LEO-PNT. Moreover, the LEO-PNT system presently relies on the GNSS, particularly for orbit determination. Consequently, our simulated LEO-PNT system is susceptible to GNSS vulnerabilities and potential failure modes. Future advancements in this domain will require the authentication of Receiver Autonomous Integrity Monitoring algorithms, exploiting the correlated faults between GNSS and LEO-PNT, thereby augmenting the robustness and assurance of the system.

We also recommend simulating the impact of signal-to-noise ratio (SNR) on the measurements. Although we have considered the measurement noises in the simulations, the SNR characterization may bring better representation of the pseudorange, carrier phase, and Doppler-shift noises, but would require simulating additional signal characteristics, antenna patterns, and modulation schemes. In addition, there are a few more effects that could improve the overall accuracy of the developed model, such as the earth orientation parameters and ocean loading. They have not been adopted due to their low impact; however, they could make the simulations even more realistic, especially in static positioning. Another point is that we have mainly focused on single-station positioning techniques, such as PPP; however, techniques using relative or differential positioning would also be relevant to simulate and check the improvement that LEO satellites can offer. We have also used Kinematic PPP techniques to compute LEOs. In real-time applications, an embedded orbit propagation model is necessary. In such scenarios, employing reduced-dynamic POD methods can offer increased efficiency by enabling data gap filling through the estimated orbits. Finally, it is recommended to apply the simulations to specific case scenarios, such as constellation planning on regional scales, which is advantageous in high latitudes, where the GNSS system encounters challenges in providing satisfactory geometry.

REFERENCES

[1] L. Wang et al., “Initial assessment of the LEO based navigation signal augmentation system from Luojia-1A satellite,” *Sensors*, vol. 18, no. 11, 2018, Art. no. 3919.

[2] Z. M. Kassas, J. J. Morales, and J. J. Khalife, “New-age satellite-based navigation STAN: Simultaneous tracking and navigation with LEO satellite signals,” *Inside GNSS Mag.*, vol. 14, no. 4, pp. 56–65, 2019.

[3] L. Wang, R. Chen, B. Xu, X. Zhang, T. Li, and C. Wu, “The challenges of LEO based navigation augmentation system–lessons learned from Luojia-1A satellite,” in *Proc. China Satell. Navigat. Conf.*, 2019, pp. 298–310.

[4] T. G. Reid et al., “Satellite navigation for the age of autonomy,” in *Proc. IEEE/ION Position, Location, Navigat. Symp.*, 2020, pp. 342–352.

[5] B. Li, H. Ge, M. Ge, L. Nie, Y. Shen, and H. Schuh, “LEO enhanced global navigation satellite system (LeGNSS) for real-time precise positioning services,” *Adv. Space Res.*, vol. 63, no. 1, pp. 73–93, 2019.

[6] H. Ge, B. Li, L. Nie, M. Ge, and H. Schuh, “LEO constellation optimization for LEO enhanced global navigation satellite system (LeGNSS),” *Adv. Space Res.*, vol. 66, no. 3, pp. 520–532, 2020.

[7] R. M. Ferre et al., “Is LEO-based positioning with mega-constellations the answer for future equal access localization?,” *IEEE Commun. Mag.*, vol. 60, no. 6, pp. 40–46, Jun. 2022.

[8] J. Khalife and Z. M. Kassas, “Assessment of differential carrier phase measurements from orbcomm LEO satellite signals for opportunistic navigation,” in *Proc. 32nd Int. Tech. Meeting Satell. Division Inst. Navigat.*, 2021, pp. 4053–4063.

[9] F. S. Prol et al., “Position, navigation, and timing (PNT) through low earth orbit (LEO) satellites: A survey on current status, challenges, and opportunities,” *IEEE Access*, vol. 10, pp. 83971–84002, 2022.

[10] O. Kodheli et al., “Satellite communications in the new space era: A survey and future challenges,” *IEEE Commun. Surv. Tut.*, vol. 23, no. 1, pp. 70–109, First Quarter 2021.

[11] H. Ge et al., “LEO enhanced global navigation satellite system (LeGNSS): Progress, opportunities, and challenges,” *Geo-Spatial Inf. Sci.*, vol. 25, no. 1, pp. 1–13, 2022.

[12] K. Çelikbilek, Z. Saleem, R. Morales Ferre, J. Praks, and E. S. Lohan, “Survey on optimization methods for LEO-satellite-based networks with applications in future autonomous transportation,” *Sensors*, vol. 22, no. 4, 2022, Art. no. 1421.

[13] X. Guo, L. Wang, W. Fu, Y. Suo, R. Chen, and H. Sun, “An optimal design of the broadcast ephemeris for LEO navigation augmentation systems,” *Geo-Spatial Inf. Sci.*, vol. 25, no. 1, pp. 34–46, 2022.

[14] L. Meng, J. Chen, J. Wang, and Y. Zhang, “Broadcast ephemerides for LEO augmentation satellites based on nonsingular elements,” *GPS Solutions*, vol. 25, no. 4, 2021, Art. no. 129.

[15] X. Xie, T. Geng, Q. Zhao, X. Liu, Q. Zhang, and J. Liu, “Design and validation of broadcast ephemeris for low earth orbit satellites,” *GPS Solutions*, vol. 22, no. 2, 2018, Art. no. 54.

[16] X. Li, Z. Jiang, F. Ma, H. Lv, Y. Yuan, and X. Li, “LEO precise orbit determination with inter-satellite links,” *Remote Sens.*, vol. 11, no. 18, 2019, Art. no. 2117.

[17] J. J. Morales, J. Khalife, U. Santa Cruz, and Z. M. Kassas, “Orbit modeling for simultaneous tracking and navigation using LEO satellite signals,” in *Proc. 32nd Int. Tech. Meeting Satell. Division Inst. Navigat.*, 2019, pp. 2090–2099.

[18] J. Saroufim, S. Hayek, and Z. M. Kassas, “Evaluation of orbit errors and measurement corrections in differential navigation with LEO satellites,” in *Proc. 36th Int. Tech. Meeting Satell. Division Inst. Navigat.*, 2023, pp. 2823–2834.

[19] R. M. Ferre, J. Praks, G. Seco-Granados, and E. S. Lohan, “A feasibility study for signal-in-space design for LEO-PNT solutions with miniaturized satellites,” *IEEE J. Miniaturization Air Space Syst.*, vol. 3, no. 4, pp. 171–183, Dec. 2022.

[20] W. Sixin, T. Xiaomei, L. Xiaohui, F. Wang, and Z. Zhuang, “Doppler frequency-code phase division multiple access technique for LEO navigation signals,” *GPS Solutions*, vol. 26, no. 3, 2022, Art. no. 98.

[21] L. Wang, Z. Lü, X. Tang, K. Zhang, and F. Wang, “LEO-augmented GNSS based on communication navigation integrated signal,” *Sensors*, vol. 19, no. 21, 2019, Art. no. 4700.

[22] X. Ren, J. Zhang, J. Chen, and X. Zhang, “Global ionospheric modeling using multi-GNSS and upcoming LEO constellations: Two methods and comparison,” *IEEE Trans. Geosci. Remote Sens.*, vol. 60, 2022, Art. no. 5800215.

[23] S. Xiong, F. Ma, X. Ren, J. Chen, and X. Zhang, “LEO constellation-augmented multi-GNSS for 3D water vapor tomography,” *Remote Sens.*, vol. 13, no. 16, 2021, Art. no. 3056.

[24] J. Xu, J. Y. Morton, D. Xu, Y. Jiao, and J. Hinks, “Tracking GNSS-like signals transmitted from LEO satellites and propagated through ionospheric plasma irregularities,” in *Proc. 36th Int. Tech. Meeting Satell. Division Inst. Navigat.*, 2023, pp. 2813–2822.

[25] M. Li, T. Xu, M. Guan, F. Gao, and N. Jiang, “LEO-constellation-augmented multi-GNSS real-time PPP for rapid re-convergence in harsh environments,” *GPS Solutions*, vol. 26, 2022, Art. no. 29.

[26] Z. Yang et al., “Real-time estimation of low earth orbit (LEO) satellite clock based on ground tracking stations,” *Remote Sens.*, vol. 12, no. 12, 2020, Art. no. 2050.

[27] R. S. Cassel, D. R. Scherer, D. R. Wilburne, J. E. Hirschauer, and J. H. Burke, “Impact of improved oscillator stability on LEO-based satellite navigation,” in *Proc. Int. Tech. Meeting Inst. Navigat.*, 2022, pp. 893–905.

[28] Z. M. Kassas and T. E. Humphreys, “Receding horizon trajectory optimization in opportunistic navigation environments,” *IEEE Trans. Aerosp. Electron. Syst.*, vol. 51, no. 2, pp. 866–877, Apr. 2015.

[29] T. R. Mortlock and Z. M. Kassas, “Performance analysis of simultaneous tracking and navigation with LEO satellites,” in *Proc. 33rd Int. Tech. Meeting Satell. Division Inst. Navigat.*, 2020, pp. 2416–2429.

[30] M. L. Psiaki, “Navigation using carrier Doppler shift from a LEO constellation: TRANSIT on steroids,” *Navigation*, vol. 68, no. 3, pp. 621–641, 2021.

[31] J. J. Morales and Z. M. Kassas, “Tightly coupled inertial navigation system with signals of opportunity aiding,” *IEEE Trans. Aerosp. Electron. Syst.*, vol. 57, no. 3, pp. 1930–1948, Jun. 2021.

[32] J. Khalife and Z. M. Kassas, “Performance-driven design of carrier phase differential navigation frameworks with megaconstellation LEO satellites,” *IEEE Trans. Aerosp. Electron. Syst.*, vol. 59, no. 3, pp. 2947–2966, Jun. 2023.

[33] C. Shi, Y. Zhang, and Z. Li, “Revisiting Doppler positioning performance with LEO satellites,” *GPS Solutions*, vol. 27, 2023, Art. no. 126.

[34] Z. M. Kassas, N. Khairallah, and S. Kozhaya, “Ad Astra: Simultaneous tracking and navigation with megaconstellation LEO satellites,” *IEEE Trans. Aerosp. Electron. Syst. Mag.*, early access, doi: 10.1109/MAES.2023.3267440.

[35] Y. Wang, B. Zhao, W. Zhang, and K. Li, “Simulation experiment and analysis of GNSS/INS/LEO/5G integrated navigation based on federated filtering algorithm,” *Sensors*, vol. 22, no. 2, 2022, Art. no. 550.

[36] L. Chen et al., “Performance evaluation of centispace navigation augmentation experiment satellites,” *Sensors*, vol. 23, no. 12, 2023, Art. no. 5704.

[37] W. Li et al., “LEO augmented precise point positioning using real observations from two CENTISPACE$^{\text{TM}}$ experimental satellites,” *GPS Solutions*, vol. 28, 2024, Art. no. 44.

[38] N. S. Miller et al., “SNAP: A Xona space systems and GPS software-defined receiver,” in *Proc. IEEE/ION Position, Location, Navigat. Symp.*, 2023, pp. 897–904.

[39] L. Ries et al., “LEO-PNT for augmenting Europe’s space-based PNT capabilities,” in *Proc. IEEE/ION Position, Location, Navigat. Symp.*, 2023, pp. 329–337.

[40] “Project indoor navigation from cubesat technology (INCUBATE),” Accessed: May, 15, 2023. [Online]. Available: https://www.incubateproject.org/

[41] A. Allahvirdi-Zadeh, K. Wang, and A. El-Mowafy, “POD of small LEO satellites based on precise real-time MADOCA and SBAS-aided PPP corrections,” *GPS Solutions*, vol. 25, 2021, Art. no. 31.

[42] A. Hauschild, O. Montenbruck, P. Steigenberger, I. Martini, and I. Fernandez-Hernandez, “Orbit determination of Sentinel-6A using the Galileo high accuracy service test signal,” *GPS Solutions*, vol. 26, 2022, Art. no. 120.

[43] Z. Tan, H. Qin, L. Cong, and C. Zhao, “Positioning using IRIDIUM satellite signals of opportunity in weak signal environment,” *Electronics*, vol. 9, no. 1, 2020, Art. no. 37.

[44] J. Khalife, M. Neinavaie, and Z. M. Kassas, “The first carrier phase tracking and positioning results with starlink LEO satellite signals,” *IEEE Trans. Aerosp. Electron. Syst.*, vol. 58, no. 2, pp. 1487–1491, Apr. 2022.

[45] T. Reid, G. René, and B. Manning, “Satellite for transmitting a navigation signal in a satellite constellation system,” U.S. Patent US2 021 024 751 9A1, 2021.

[46] L. Cheng, Y. Dai, W. Guo, and J. Zheng, “Structure and performance analysis of signal acquisition and Doppler tracking in LEO augmented GNSS receiver,” *Sensors*, vol. 21, no. 2, 2021, Art. no. 525.

[47] A. M. El-Naggar, “New method of GPS orbit determination from GCPS network for the purpose of DOP calculations,” *Alexandria Eng. J.*, vol. 51, no. 2, pp. 129–136, 2012.

[48] J.-C. Yoon, B.-S. Lee, and K.-H. Choi, “Spacecraft orbit determination using GPS navigation solutions,” *Aerosp. Sci. Technol.*, vol. 4, no. 3, pp. 215–221, 2000.

[49] T. G. Reid, T. Walter, P. K. Enge, and T. Sakai, “Orbital representations for the next generation of satellite-based augmentation systems,” *GPS Solutions*, vol. 20, pp. 737–750, 2016.

[50] P. Willis, F. Deleflie, F. Barlier, Y. Bar-Sever, and L. Romans, “Effects of thermosphere total density perturbations on LEO orbits during severe geomagnetic conditions (Oct.–Nov. 2003) using DORIS and SLR data,” *Adv. Space Res.*, vol. 36, no. 3, pp. 522–533, 2005.

[51] D. M. Sanchez, A. F. Prado, and T. Yokoyama, “On the effects of each term of the geopotential perturbation along the time I: Quasi-circular orbits,” *Adv. Space Res.*, vol. 54, no. 6, pp. 1008–1018, 2014.

[52] V. U. Nwankwo, S. K. Chakrabarti, and R. S. Weigel, “Effects of plasma drag on low earth orbiting satellites due to solar forcing induced perturbations and heating,” *Adv. Space Res.*, vol. 56, no. 1, pp. 47–56, 2015.

[53] J. L. C. Rodríguez et al., “Poliastro 0.17.0 (SciPy US ’22 edition),” *Zenodo*, Jul. 2022, doi :10.5281/zenodo.17462.

[54] M. G. Matossian, “Improved candidate generation and coverage analysis methods for design optimization of symmetric multisatellite constellations,” *Acta Astronaut.*, vol. 40, no. 2, pp. 561–571, 1997.

[55] J. Wang, L. Li, and M. Zhou, “Topological dynamics characterization for LEO satellite networks,” *Comput. Netw.*, vol. 51, no. 1, pp. 43–53, 2007.

[56] T. G. Reid, A. M. Neish, T. Walter, and P. K. Enge, “Broadband LEO constellations for navigation,” *Navigation*, vol. 65, no. 2, pp. 205–220, 2018.

[57] R. Santerre, A. Geiger, and S. Banville, “Geometry of GPS dilution of precision: Revisited,” *GPS Solutions*, vol. 21, no. 4, pp. 1747–1763, 2017.

[58] W. Schreiner et al., “COSMIC-2 radio occultation constellation: First results,” *Geophys. Res. Lett.*, vol. 47, no. 4, 2020, Art. no. e2019GL086841.

[59] V. V. Forsythe, T. Duly, D. Hampton, and V. Nguyen, “Validation of ionospheric electron density measurements derived from spire CubeSat constellation,” *Radio Sci.*, vol. 55, no. 1, 2020, Art. no. e2019RS006953.

[60] G. W. Huang, Q. Zhang, and G. C. Xu, “Real-time clock offset prediction with an improved model,” *GPS Solutions*, vol. 18, no. 1, pp. 95–104, 2014.

[61] K. Wang and A. El-Mowafy, “LEO satellite clock analysis and prediction for positioning applications,” *Geo-Spatial Inf. Sci.*, vol. 25, no. 1, pp. 14–33, 2022.

[62] A. Allahvirdi-Zadeh, J. Awange, A. El-Mowafy, T. Ding, and K. Wang, “Stability of CubeSat clocks and their impacts on GNSS radio occultation,” *Remote Sens.*, vol. 14, no. 2, 2022, Art. on. 362.

[63] N. Ashby, “Relativity in the global positioning system,” *Living Rev Relativity*, vol. 6, no. 1, pp. 1–42, 2003.

[64] S. Han and J. Wang, “Integrated GPS/INS navigation system with dual-rate Kalman filter,” *GPS Solutions*, vol. 16, pp. 389–404, Jul., 2012.

[65] J. Geng and Y. Bock, “Triple-frequency GPS precise point positioning with rapid ambiguity resolution,” *J. Geodesy*, vol. 87, no. 5, pp. 449–460, 2013.

[66] T. Takasu and A. Yasuda, “Development of the low-cost RTK-GPS receiver with an open source program package RTKLIB,” in *Proc. Int. Symp. GPS/GNSS*, 2009, pp. 1–6.

[67] Y. Xiang, Z. Xu, Y. Gao, and W. Yu, “Understanding long-term variations in GPS differential code biases,” *GPS Solutions*, vol. 24, no. 4, 2020, Art. no. 118.

[68] N. Wang, Y. Yuan, Z. Li, O. Montenbruck, and B. Tan, “Determination of differential code biases with multi-GNSS observations,” *J. Geodesy*, vol. 90, no. 3, pp. 209–228, 2016.

[69] J. Sanz, J. Miguel Juan, A. Rovira-Garcia, and G. González-Casado, “GPS differential code biases determination: Methodology and analysis,” *GPS Solutions*, vol. 21, no. 4, pp. 1549–1561, 2017.

[70] J. Paziewski and P. Wielgosz, “Accounting for Galileo–GPS intersystem biases in precise satellite positioning,” *J. Geodesy*, vol. 89, pp. 81–93, 2015.

[71] F. d. S. Prol, P. d. O. Camargo, J. F. G. Monico, and M. T. d. A. H. Muella, “Assessment of a TEC calibration procedure by single-frequency PPP,” *GPS Solutions*, vol. 22, no. 2, 2018, Art. no. 35.

[72] O. Montenbruck, A. Hauschild, and P. Steigenberger, “Differential code bias estimation using multi-GNSS observations and global ionosphere maps,” *Navigation*, vol. 61, no. 3, pp. 191–201, 2014.

[73] P. A. Iannucci and T. E. Humphreys, “Fused low-earth-orbit GNSS,” *IEEE Trans. Aerosp. Electron. Syst.*, early access, doi: 10.1109/TAES.2022.3180000.

[74] D. Van Buren, P. Axelrad, and S. Palo, “Design of a high-stability heterogeneous clock system for small satellites in LEO,” *GPS Solutions*, vol. 25, 2021, Art. no. 105.

[75] E. D. Kaplan and C. J. Hegarty, *Understanding GPS: Principles and Applications*, 2nd ed. Norwood, MA, USA: Artech House, 2006.

[76] J. T. Wu, S. C. Wu, G. A. Hajj, W. I. Bertiger, and S. M. Lichten, “Effects of antenna orientation on GPS carrier phase,” *Manuscripta Geodaetica*, vol. 18, pp. 91–98, 1993.

[77] W. Chen, C. Hu, S. Gao, Y. Chen, and X. Ding, “Error correction models and their effects on GPS precise point positioning,” *Surv. Rev.*, vol. 41, no. 313, pp. 238–252, 2009.

[78] J. Yuan et al., “Impact of attitude model, phase wind-up and phase center variation on precise orbit and clock offset determination of GRACE-FO and CentiSpace-1,” *Remote Sens.*, vol. 13, no. 13, 2021, Art. no. 2636.

[79] J. Klobuchar, “Ionospheric time-delay algorithms for single-frequency GPS users,” *IEEE Trans. Aerosp. Electron. Syst.*, vol. AES-23, no. 3, pp. 325–331, May 1987.

[80] Y. Yuan, N. Wang, Z. Li, and X. Huo, “The BeiDou global broadcast ionospheric delay correction model (BDGIM) and its preliminary performance evaluation results,” *Navigation*, vol. 66, pp. 55–69, 2019.

[81] M. Hernández-Pajares et al., “The IGS VTEC maps: A reliable source of ionospheric information since 1998,” *J. Geodesy*, vol. 83, pp. 263–275, 2009.

[82] F. S. Prol, A. G. Smirnov, M. M. Hoque, and Y. Y. Shprits, “Combined model of topside ionosphere and plasmasphere derived from radio-occultation and Van Allen Probes data,” *Sci. Rep.*, vol. 12, no. 1, 2022, Art. no. 9732.

[83] F. S. Prol and M. M. Hoque, “A tomographic method for the reconstruction of the plasmasphere based on COSMIC/ FORMOSAT-3 data,” *IEEE J. Sel. Topics Appl. Earth Observ. Remote Sens.*, vol. 15, pp. 2197–2208, 2022.

[84] M. M. Hoque, N. Jakowski, and F. S. Prol, “A new climatological electron density model for supporting space weather services,” *J. Space Weather Space Climate*, vol. 12, 2022, Art. no. 1.

[85] F. S. Prol, T. Kodikara, M. M. Hoque, and C. Borries, “Global-scale ionospheric tomography during the Mar. 17, 2015 geomagnetic storm,” *Space Weather*, vol. 19, no. 12, 2021, Art. no.e2021SW002889.

[86] J. P. Collins, “Assessment and development of a tropospheric delay model for aircraft users of the global positioning system,” Dept. Geodesy Geomatics Eng., Univ. New Brunswick, Fredericton, NB, Canada, Tech. Rep. 203, 1999.

[87] G. Möller, R. Weber, and J. Böhm, “Improved troposphere blind models based on numerical weather data,” *Navigation*, vol. 61, no. 3, pp. 203–211, 2014.

[88] J. Askne and H. Nordius, “Estimation of tropospheric delay for microwaves from surface weather data,” *Radio Sci.*, vol. 22, no. 3, pp. 379–386, 1987.

[89] C. Qiu et al., “The performance of different mapping functions and gradient models in the determination of slant tropospheric delay,” *Remote Sens.*, vol. 12, no. 1, 2020, Art. no. 130.

[90] K. Selvan, A. Siemuri, F. S. Prol, P. Välisuo, H. B. M. Zahidul, and H. Kuusniemi, “Precise orbit determination of LEO satellites: A systematic review,” *GPS Solutions*, vol. 27, 2023, Art. no. 178.

[91] B. W. Remondi, “Computing satellite velocity using the broadcast ephemeris,” *GPS Solutions*, vol. 8, no. 3, pp. 181–183, 2004.

[92] Y. Feng and Y. Zheng, “Efficient interpolations to GPS orbits for precise wide area applications,” *GPS Solutions*, vol. 9, no. 4, pp. 273–282, 2005.

[93] A. Rovira-Garcia, J. Juan, J. Sanz, G. González-Casado, and E. Bertran, “Fast precise point positioning: A system to provide corrections for single and multi-frequency navigation,” *Navigation*, vol. 63, no. 3, pp. 231–247, 2016.

[94] R. F. Leandro, M. C. Santos, and R. B. Langley, “Analyzing GNSS data in precise point positioning software,” *GPS Solutions*, vol. 15, no. 1, pp. 1–13, 2011.

[95] J. Kouba and P. Héroux, “Precise point positioning using IGS orbit and clock products,” *GPS Solutions*, vol. 5, no. 2, pp. 12–28, 2001.

Fabricio S. Prol received the Ph.D. degree in cartographic sciences (with focus on geodetic remote sensing and geodetic positioning) from São Paulo State University, São Paulo, Brazil, in 2019.

Since 2021, he has been with the Finnish Geospatial Research Institute, National Land Survey of Finland, Espoo, Finland. His research interests include low earth orbit positioning, navigation, and timing systems, ionospheric modeling, global navigation satellite system positioning, and data assimilation.

M. Zahidul H. Bhuiyan received a Ph.D. degree in communications engineering from the Tampere University of Technology (TUT), Tampere, Finland, in 2007.

He is a Research Professor with the Department of Navigation and Positioning, Finnish Geospatial Research Institute, National Land Survey of Finland, Espoo, Finland. He is also a Technical Expert with the European Union Agency for the Space Programme, Prague, Czech Republic, in H2020 project reviewing and proposal evaluation. He is actively involved in teaching global navigation satellite system (GNSS)-related courses in Finnish universities and other training schools. His main research interests include multi-GNSS receiver development, positioning, navigation, and timing robustness and resilience, and seamless positioning.

Sanna Kaasalainen received a Ph.D. degree in astronomy from the University of Helsinki, Helsinki, Finland, in 2003.

She is a Professor and Head of the Department of Navigation and Positioning, Finnish Geospatial Research Institute, National Land Survey of Finland, Espoo, Finland. She has research experience in lidar remote sensing, sensor development, and astronomy. Her research interests include resilient positioning, navigation, and timing, situational awareness, and optical sensors.

E. Simona Lohan (Senior Member, IEEE) received the M.Sc. degree in electrical engineering from the Politehnica University of Bucharest, Bucharest, Romania, in 1997, the D.E.A. degree (French equivalent of master) in econometrics from Ecole Polytechnique, Paris, France, in 1998, and the Ph.D. degree in telecommunications from the Tampere University of Technology, Tampere, Finland, in 2003.

She is currently a Professor with the Electrical Engineering Unit, Tampere University, Tampere, and the Coordinator of the MSCA EU "A-WEAR" Network. Her current research interests include global navigation satellite systems, low earth orbit positioning, navigation, and timing, wireless location techniques, wearable computing, and privacy-aware positioning solutions.

Jaan Praks received the B.Sc. degree in physics from the University of Tartu, Tartu, Estonia, in 1996, and the D.Sc. (Tech.) degree in space technology and remote sensing from Aalto University, Espoo, Finland, in 2012.

He is currently an Assistant Professor of Electrical Engineering with the Department of Electronics and Nanoengineering, School of Electrical Engineering, Aalto University. He works on microwave remote sensing, scattering modeling, microwave radiometry, hyperspectral imaging, and advanced synthetic aperture radar techniques, such as polarimetry, interferometry, polarimetric interferometry, and tomography. One of the most visited topics in his research is remote sensing of boreal forest. He led project that produced two first Finnish satellites. He has been involved also in spinning off several companies in the field of satellite remote sensing. He is a Principal Investigator of several small satellite missions. His research interests include emerging nanosatellite technology.

Dr. Praks is an Active Member of Scientific Community, a Member of the Finnish National Committee of COSPAR, the Chairman of the Finnish National Committee of URSI, and the Chair and Co-Chair of many national and international conferences. His research team is a Member of the Finnish Centre of Excellence in Research of Sustainable Space.

Kaan Çelikbilek received the B.Sc. (Tech.) degree in electrical and electronics engineering from Bilkent University, Ankara, Türkiye, in 2018, and the M.Sc. (Tech.) degree in robotics and artificial intelligence in 2020 from Tampere University, Tampere, Finland, where he is currently working toward the Ph.D. degree in computing and electrical engineering.

His research interests include deep learning, reinforcement learning, multiobjective optimization, satellite communication, and robotics.

Heidi Kuusniemi (Member, IEEE) received the M.Sc. (Tech.) degree (with distinction) and the D.Sc. (Tech.) degree from the Tampere University of Technology, Finland, in 2002 and 2005, respectively, both in information technology.

She is currently the Director of the Digital Economy Research Platform and a Professor of Computer Science with the University of Vaasa, Vaasa, Finland; a Research Professor with the Finnish Geospatial Research Institute, National Land Survey of Finland, Espoo, Finland; and an Adjunct Professor of Satellite Navigation with Tampere University, Tampere, and Aalto University, Espoo. She has more than 20 years of experience in research and development of positioning technologies and has held many significant positions of trust and expertise in the global scientific navigation community. In 2017, she was a visiting Scholar with GPS Laboratory, Stanford University, Stanford, CA, USA. Part of her doctoral research was conducted at the University of Calgary, Department of Geomatics Engineering, Canada. Her research interests include global navigation satellite systems, especially reliability, estimation and data fusion, mobile precision positioning with applications, indoor localization and opportunities of positioning, navigation, and timing in new space.

Dr. Kuusniemi was a Member of the Research Council for Natural Sciences and Engineering with the Academy of Finland from 2019 to 2021.